A Reliable Procedure to Estimate the Rupture Propagation Directions from Source Directivity: The 2016–2018 Central Italy Seismic Sequence

Giovanna Calderoni*[1], Rita Di Giovambattista[1], and Guido Ventura[1]

Abstract

We present a new approach to estimate the predominant direction of rupture propagation during a seismic sequence. A fast estimation of the rupture propagation direction is essential to know the azimuthal distribution of shaking around the seismic source and the associated risks for the earthquake occurrence. The main advantage of the proposed method is that it is conceptually reliable, simple, and fast (near real time). The approach uses the empirical Green's function technique and can be applied directly to the waveforms without requiring the deconvolution of the instrumental response and without knowing a priori the attenuation model and the orientation of the activated fault system. We apply the method to the 2016–2017 Amatrice-Visso-Norcia high-energy and long-lasting earthquake series in central Italy, which affected a large area up to 80 km along strike, with more than 130,000 events of small-to-moderate magnitude recorded until the end of August 2022. Most of the selected events analyzed in this study have a magnitude greater than 4.4 and only four seismic events have a magnitude in the range of 3.3–3.7. Our results show that the complex activated normal fault system has a rupture direction mainly controlled by the pre-existing normal faults and by the orientation of the reactivated faults. In addition, the preferred direction of rupture propagation is also controlled by the presence of fluid in the pre-existing structural discontinuities. We discuss the possible role of fluids as a cause of bimaterial interface. Another important finding from our analysis is that the spatial evolution of seismicity is controlled by the directivity.

Cite this article as Calderoni, G., R. Di Giovambattista, and G. Ventura (2023). A Reliable Procedure to Estimate the Rupture Propagation Directions from Source Directivity: The 2016–2018 Central Italy Seismic Sequence, *Seismol. Res. Lett.* **XX**, 1–13, doi: 10.1785/0220220318.

Supplemental Material

Introduction

Rupture directivity is a key factor in ground motion and the associated risk leading to significant amplifications in the forward rupture propagation direction and deamplifications in the backward direction. The directional effect (Douglass *et al.*, 1988), which can have catastrophic effects on the azimuthal distribution of damage in the epicentral area of strong seismic events, has also been observed in moderate events. Different approaches to the study of source directivity are described in the literature. Some authors used source, path, and site deconvolution to model the azimuthal variations of the rupture propagation direction, whereas other authors used the empirical Green's function (EGF) technique to deconvolve the signal from the transfer function of the sensor, from the crustal attenuation effects of the path and of the site. Using the spectral ratios estimated for each station, the site-specific amplification or attenuation is taken into account and a more accurate representation of ground motion is obtained. The target and EGF event pair must be co-located to have the same path from source to station. The directivity has been observed in many different areas for medium (Seekins and Boatwright, 2010) and small (e.g., Tomic *et al.*, 2009; Chen *et al.*, 2010; Kurzon *et al.*, 2014; Ross and Ben-Zion, 2016; Folesky *et al.*, 2016) earthquakes. The directivity has also been analyzed for recent earthquakes in Italy. The 1997 seismic sequence in Umbria and Marche (M_w 5.5) was studied by Pino *et al.* (1999) and Cultrera *et al.* (2008), the 2002 M_w 5.7 Molise earthquake by Gorini *et al.* (2004), and the 2009 L'Aquila earthquake by Malagnini *et al.* (2012), Akinci *et al.* (2010), Tinti *et al.* (2014), and Calderoni *et al.* (2015). Directivity appears to be a feature of some fault systems. Calderoni *et al.* (2017) have shown that

1. Istituto Nazionale di Geofisica e Vulcanologia, Rome, Italy, https://orcid.org/0000-0001-5622-1396 (RDG); https://orcid.org/0000-0001-9388-9985 (GV)

*Corresponding author: giovanna.calderoni@ingv.it

the same area activated during the L'Aquila 2009 and Amatrice 2016–2017 seismic sequences had the same preferred rupture propagation direction. In this study, we present a new approach aimed at generalizing the statistical procedure proposed by Calderoni *et al.* (2017) to estimate the rupture directivity of the strongest earthquakes ($M_w \geq 4.4$) of the 2016–2017 seismic sequence in central Italy. Other authors investigated the effect of source directivity for the same seismic sequence using different methods. Calderoni *et al.* (2017) analyzed 16 events with magnitudes greater than 4.4 by using an EGF approach. Wang *et al.* (2019) analyzed the directivity of 36 events using the azimuthal variation of source spectra, the known site response functions, and propagation path attenuation. Convertito *et al.* (2017) and Pischiutta *et al.* (2016) analyzed the directivity of the 24 August M_w 5.97 earthquake using the azimuthal variation of peak ground velocity (PGV) and peak ground acceleration (PGA). Furthermore, Colavitti *et al.* (2022) studied the directivity of a large sector of the central Apennines including the seismic sequences of L'Aquila 2009 and Amatrice 2016–2017. In many of these studies, the parameterization of directivity is determined by a simple unilateral (Haskell, 1964) or bilateral (Boatwright, 2007) theoretical dispersion model with nonlinear least-squares problems. In these methods, the choice of variables must be carefully considered to reduce the strong trade-off between some fitting parameters. Here, we study the azimuthal distribution of ground motions due to directivity effects by analyzing the azimuthal variations of the high-frequency spectral splitting.

Our method is an extension of the approach proposed by Calderoni *et al.* (2017), which is based on the EGF in the frequency domain. Although Calderoni *et al.* (2017) detects unilateral and bilateral ruptures along the strike of the main, northwest–southeast-striking fault system, the method presented here detects the directions of the predominant rupture on the whole solid angle without assumptions on the orientation of the activated fault system. In this study, we focused on evaluating the along-strike directivity of earthquakes using stations in the orthogonal directions. However, this approach does not provide insights into up-dip or down-dip directivity. The analysis method is based on recordings from stations located at a minimum distance of 10 km from the earthquakes. This requirement ensures that the signals are not saturated and that nonlinearity effects from the source are excluded. However, it also means that the effects of up-dip or down-dip directivity cannot be evaluated with this method.

In central Italy, major seismic events occur mainly along northwest–southeast-striking normal faults. For this reason, Calderoni *et al.* (2017) performed an analysis of the along-strike rupture directivity by grouping stations according to their azimuthal position within an angle of ±45° from the fault strike. The stations are located on both sides of the fault and were divided into three groups: north-northwest, south-southeast, and fault orthogonal (FO). To generalize this procedure, we assume here that the faults have different orientations and estimate the rupture direction over the whole solid angle (0°–360°) with an error of ±30° depending on the station azimuthal coverage. We apply this new procedure to 50 seismic events of the Amatrice-Visso-Norcia (AVN) seismic sequence in central Italy 2016–2017. Events have $M_w \geq 4.4$ and four with $3.3 < M_w < 3.7$. A study by Wang *et al.* (2019) investigated the rupture directivity of 36 events of the same seismic sequence using the azimuthal variation of apparent source spectra by knowing the site response functions and propagation path attenuation. Compared to previous methods, our method has some advantages: it is a simple method that allows a quick estimate of rupture directivity and can be applied anywhere, even if you do not know the main directions of the fault system. We do not apply any corrections to estimate the site response functions and the attenuation of the propagation path. Moreover, thanks to the estimation of directivity by splitting spectral ratios rather than by azimuthal variation of corner frequencies (Wang *et al.*, 2019), our method is independent of the choice of spectral model (which is usually too simplified to represent reality). To verify the accuracy of our method, we compare our results with those obtained by Calderoni *et al.* (2017), Wang *et al.* (2019), and Convertito *et al.* (2017). The identification of the main direction of the rupture propagation has received a lot of attention in recent years because it has a significant impact on strong ground motions and on the migration of earthquakes. Therefore, the results of this study have important clues to hazard scenarios and could lead to a more refined hazard assessment of the studied region providing additional information for earthquake prediction models.

Geological and Seismological Background

The geodynamics setting of central Italy is characterized by the westward subduction of the Adriatic plate below the northwest–southeast-striking Apennine's fold-and-thrust belts and the Tyrrhenian Sea back-arc, which is characterized by a thinned continental crust and oceanic sub-basins. The crustal thickness increases moving eastward from the Tyrrhenian Sea side, where it is about 10–20 km, to the Adriatic foreland, where it reaches 30–35 km (Carminati and Doglioni, 2012). The eastward opening of the Tyrrhenian back-arc is associated with the eastward migration of the compressive front of the Apennines (Di Luccio *et al.*, 2010). From Plio-Pleistocene times up to now, the axial sector of the Central Apennines, which is located above the flexure of the Adriatic subduction slab, is affected by a northeast–southwest extension that produced a set of intramountain basins bounded by northwest–southeast-striking, active normal faults (Ventura *et al.*, 2007). Active compressive deformation occurs west of the Apennine chain axis. Central Apennines consist of thrust overlying Meso-Cenozoic carbonates and Miocenic flysch (Billi and Tiberti, 2009, and references therein). Intermountain basins and seismogenic, northwest–southeast-

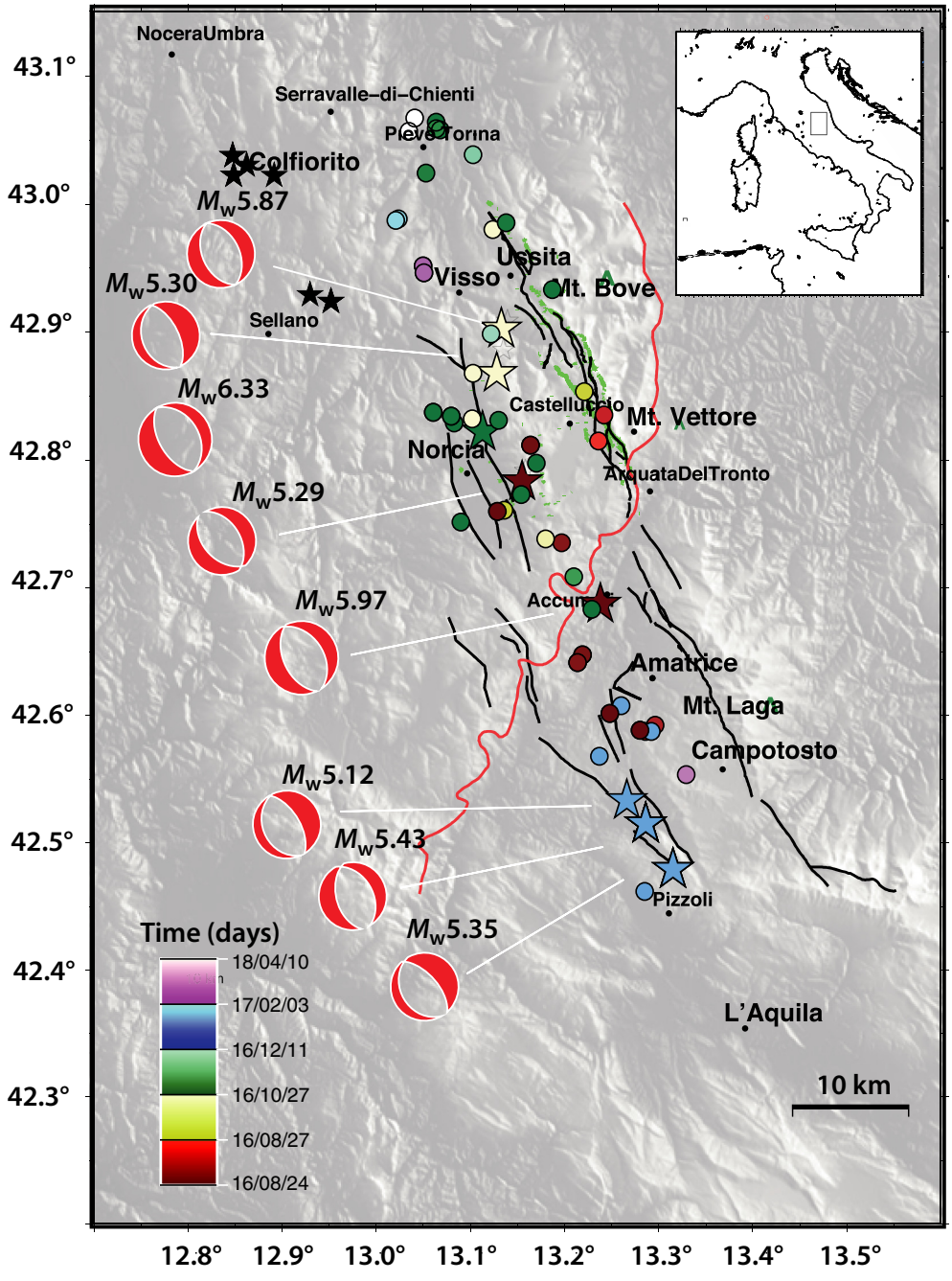

Figure 1. Map of the study area. Stars ($M_w > 5$) and circles ($M_w < 5$) represent the epicenters of the seismic events analyzed in this study. In the top right inset map of Italy, the rectangle shows the location of the analyzed area. The color scale of the epicenter symbols corresponds to the time evolution of the seismicity. The black lines are the mapped normal faults from Pucci *et al.* (2017). The red line is the Sibillini thrust front. The left side focal mechanism plots represent the fault plane solutions of the $M_w > 5$. The color version of this figure is available only in the electronic edition.

striking normal faults bound the main Plio-Quaternary intramountain Apennine basins filled by continental sediments (Fig. 1). The Sibillini thrust is north-northeast–south-southwest-striking and brought the internal Meso-Cenozoic formations on the more external Cretaceous–Paleogenic units (Billi and Tiberti, 2009). The seismicity of the Central Apennines occurs within the first 10–15 km of the crust and concentrates along the chain axis with events of magnitude up to 7 (see Data and Resources). The focal mechanisms indicate normal movements along northwest–southeast-striking planes (Montone and Mariucci, 2016). It has been proposed that some of the more recent Central Apennines seismic sequences are modulated by the release of CO_2-rich fluids (Chiodini *et al.*, 2004, 2020; Miller *et al.*, 2004; Di Luccio *et al.*, 2010; Malagnini *et al.*, 2012). Chiodini *et al.* (2020) find a positive correlation between CO_2 release and the number and energy of earthquakes occurring during the 2016–2017 AVN seismic sequence, which includes four mainshocks with M_w between 5.4 and 6.5. This sequence is characterized by events shallower than 10–15 km depth aligned along a northwest–southeast direction. A low number of aftershocks has been also observed between the areas of the Norcia and Amatrice main events in the area of the north-northeast–south-southwest-striking Sibillini thrust. The more energetic AVN events ($M_w > 5$) ruptured the surface and reactivated northwest–southeast-striking normal faults. The dip-slip focal mechanisms are consistent with this kinematics and fault strike (Mariucci and Montone, 2020). According to Chiarabba *et al.* (2018), the AVN sequence developed in a sector of the Central Apennines characterized by high-V_P/V_S values between 3 and 6 km; the high-V_P/V_S volume is interpreted as a northwest–southeast elongated zone of overpressurized fluids mainly located at the base of the upper crust in the hanging wall of the main normal faults.

Data and Method

We use the waveforms recorded by 24-bit broadband seismological stations (mostly 40 s Nanometrics Trillium) of the Italian Seismic Network operated by the Istituto Nazionale di Geofisica e Vulcanologia (INGV), located at source distances ranging from 10 to 250 km. The waveforms of the events, their hypocentral parameters, and magnitudes are available online (see Data and Resources).

In this study, we consider the 16 target-EGF pairs analyzed by Calderoni *et al.* (2017) adding 1–4 new EGF for each pair. A maximum epicentral distance of 5 km between the target event and EGFs is chosen. We also add an additional 34 target events with $M_w \geq 4.0$ and four events with $3.3 < M_w < 3.7$ and the associated 1–3 EGFs. The target and EGF event pair must be co-located to have the same path from source to station. We selected closely located, well-recorded EGF events (following Abercrombie, 2014, 2015) to use in the spectral ratio analysis. Moment magnitudes are taken from the moment tensor website (see Data and Resources). For the majority of the EGFs, the moment tensor solution is not available. In these cases, the local magnitudes (M_L) are taken from the INGV Bulletin (see Data and Resources). Seismograms are processed using a generalized procedure modified from Calderoni *et al.* (2017). The amplitude spectra are computed by a fast Fourier transform in a time window of 10 s starting 1 s before the arrival of the direct *S* wave. This window includes the most energetic part of the *S* phase of the two horizontal components. The selected time windows are tapered with a conventional Hanning taper in the Seismic Analysis Code (SAC) software suite, and the spectra are smoothed with a 0.1 Hz wide triangular operator in the same package (Goldstein *et al.*, 2003). To estimate the rupture directivity, we apply the EGF method (e.g., Hartzell, 1978; Frankel and Kanamori, 1983; Ammon *et al.*, 1993; Mori, 1993; Hough and Dreger, 1995; Fletcher and Spudich, 1998; Lanza *et al.*, 1999; McGuire, 2004; Calderoni *et al.*, 2017). The EGF approach assumes a target event and a smaller EGF event located at a similar location and having a similar focal mechanism. In this condition both seismic events share nearly the same propagation effect, and there is a linear scaling between their source terms at the same stations. However, when using different EGFs the results may not be the same (Prieto *et al.*, 2006; Kane *et al.*, 2013; Del Gaudio *et al.*, 2015). For this reason, it is better to use multiple EGFs. In this approach we employ the EGF deconvolution technique and introduce some changes compared to Calderoni *et al.* (2017), as described subsequently. Following Ross and Ben-Zion (2016), we used a *t*-test criterion to statistically evaluate the mean spectral ratio separation between the three groups of stations located forward, backward, and FO or in any azimuthal direction, and we estimate the following statistical parameter (t_{ij}(Azi)) in a frequency range between the target and EGF corner frequencies (F_{min}, F_{max}) identified by visual inspection:

$$t_{ij}(\mathrm{Azi}) = \frac{\underline{X_i} - \underline{X_j}}{s_{\underline{X_i}-\underline{X_j}}}, \tag{1}$$

$$s_{\underline{X_i}-\underline{X_j}} = \sqrt{\frac{s_i^2}{n_i} + \frac{s_j^2}{n_j}}, \tag{2}$$

in which Azi varies from 0° to 180° with a step of 5°, $i, j = 1, 2, 3$ in which $i \neq j$ represent the three station groups, $\underline{X_i}$ is the geometric mean of the spectral ratios, s_i is the standard deviation for each group of stations in the (F_{min}, F_{max}) frequency range. The target and EGF corner frequencies (F_{min}, F_{max}) correspond to the asymptotes of the spectral ratio at low and high frequencies. The estimation of the target event's directivity is performed by considering the frequency band between the corner frequencies of the target and EGF, ensuring that any directivity of the EGF does not influence the analysis. There is no bias in the directivity index if F_{min} and F_{max} are chosen slightly smaller or slightly larger than the target and/or EGF corner frequencies, respectively. Calderoni *et al.* (2017) have shown that reducing F_{min} by 20% and increasing F_{max} by 20% results in a change in the directivity index of less than 10%.

An index of directivity (D_{ij}) is then calculated as the average over this frequency range:

$$D_{ij} = \frac{1}{F_{max} - F_{min}} \int_{F_{min}}^{F_{max}} t_{ij}(f)\mathrm{d}f. \tag{3}$$

Unlike in Ross and Ben-Zion (2016) and Calderoni *et al.* (2017), we also consider the azimuthal direction in which D_{ij} is less than 2 to determine the maximum value of D_{ij} corresponding to the main rupture direction. At least three stations in the four investigated azimuthal directions are needed.

The directivity index (D_{index}) and the azimuth (Azi_{evt}) of the main rupture direction associated to the seismic event (Table S3, available in the supplemental material to this article) are computed as an average over the target-EGF pairs using a weighted directivity index (Table S1). Following Ross and Ben-Zion (2016), a value of approximately 2.0 for the directivity index is a reliable threshold for indicating significantly different samples. In this study, we want also to consider the small variation of the directivity index. For this reason, we have chosen to weight (Table S1) this parameter by associating a weight of 0.25 for a reduction of up to 50% of the threshold value (equal to 1), a weight of 0.50 for a reduction of up to 10% (equal to 1.8), a weight of 0.75 for a 50% increase (equal to 3), and a weight of 1 for a greater than 50% increase (greater than 3).

$$D_{\mathrm{index},i} = \frac{\sum_k^1 D_{ij} w_k}{\sum_k^1 w_k}, \tag{4}$$

$$\mathrm{Azi}_{\mathrm{evt},i} = \frac{\sum_k^1 \mathrm{Azi}_{ij} w_k}{\sum_k^1 w_k}. \tag{5}$$

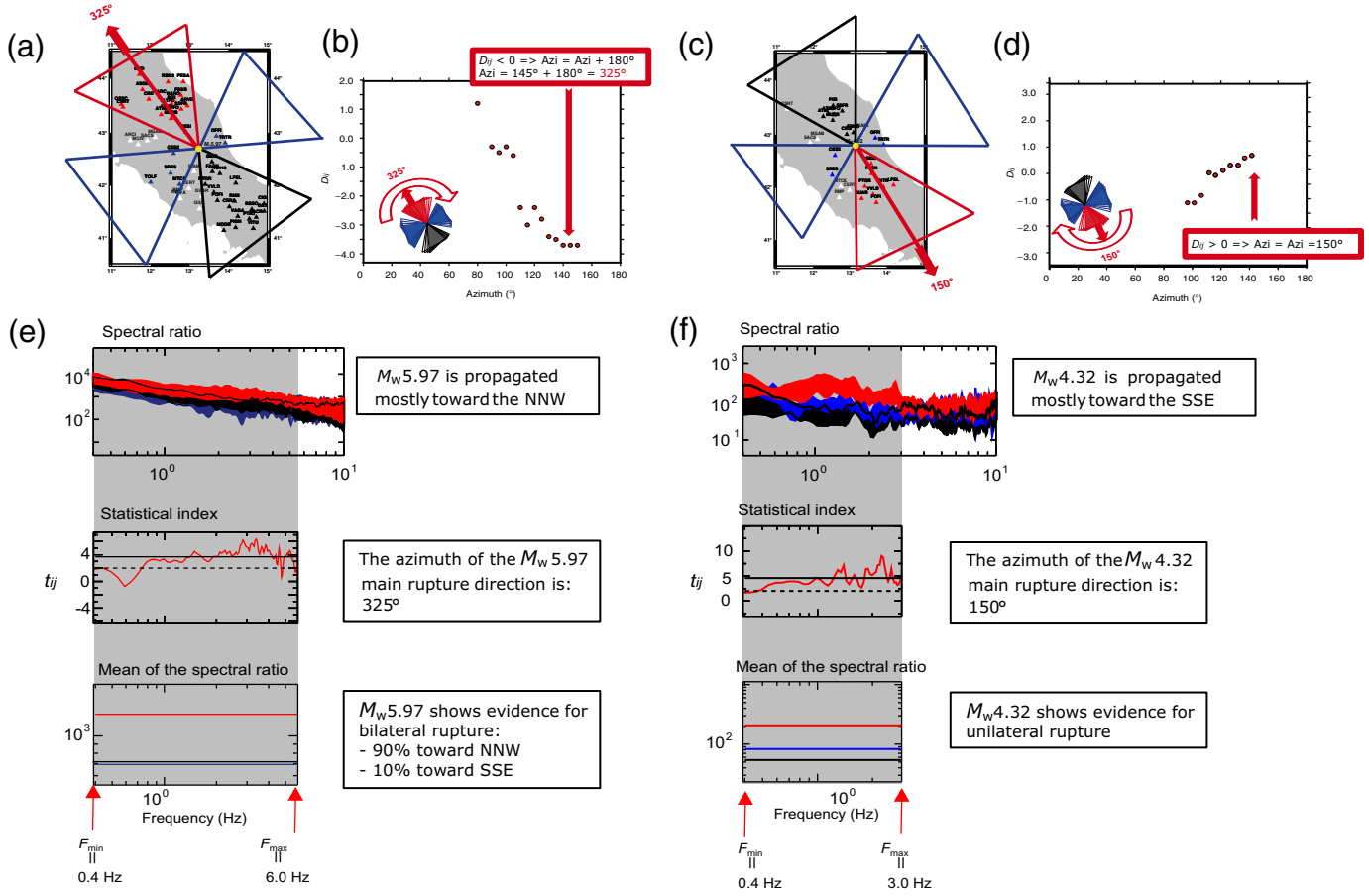

Figure 2. Schematic illustration of the result of the method applied to the (a,b,e) Amatrice M_w 5.97 and (c,d,f) M_w 4.32 and empirical Green's function (EGF) pair of events. (a,c) Map of the stations in the forward (red), backward (black), and fault orthogonal (FO, blue) directions. (b,d) Azimuthal variation of the directivity index (D_{ij}). (e,f) In the top, azimuthal variations in the ±1 standard deviation band around the mean of the spectral ratios at different azimuths (red, black, and blue curves are relative to forward, backward, and FO station groups, respectively); in the middle, the t_{ij} curves provide statistical estimates of the spectral separation between the different directions; and in the bottom left and right, the mean of the spectral ratios indicate a bilateral and unilateral rupture, respectively. The color version of this figure is available only in the electronic edition.

Figure 2 shows a schematic representation of the method applied to the event pair Amatrice M_w 5.97 and M_w 4.32 and EGF. The azimuthal coverage of the stations is not uniform with an azimuthal gap between 0° and about 80° (Fig. 2a,b). This problem, which depends on the geometric distribution of the stations, affects many of the events analyzed in the 2016–2017 sequence in central Italy. For this reason, for the application of the method we grouped the stations within ±30° for each azimuthal direction investigated. With a better azimuthal coverage, we could have reduced this range by greatly increasing the potential of the method by reducing the uncertainty of the estimated directivity.

However, because the Apennine fault systems are mainly oriented in the northwest–southeast direction, we can also constrain the predominant rupture direction propagation using an azimuthal station coverage, which is not optimized. As can be seen in Figure 2, the estimated D_{ij} depends on the choice of stations grouped in the different azimuths and on the choice of the frequency band in which D_{ij} is estimated, which corresponds to the frequency range between the spectral ratio low- and high-frequency asymptotes (F_{min} and F_{max} in Fig. 2e). However, the frequency band affects the D_{ij} value but not the rupture propagation direction. The relative amplitude of the spectral ratios between F_{min} and F_{max} is a clear indicator of unilateral or bilateral rupture; the FO curve is in the middle range for a unilateral rupture (Fig. 2f), whereas it is minimal for a bilateral rupture (Fig. 2d).

We show that our results are stable when using different EGF (Table S2, Fig. S1). The results showed a high stability of the rupture directivity estimate as the EGF was varied (Table S2, Fig. S1). As regards the influence of the spatial distribution of the stations, from Table S2 we can see that the results show stability for the different target-EGF pair and varying the number of stations selected in the three directions of analysis (forward, backward, and FO). However, in some cases the directivity index can change as the target-EGF pair

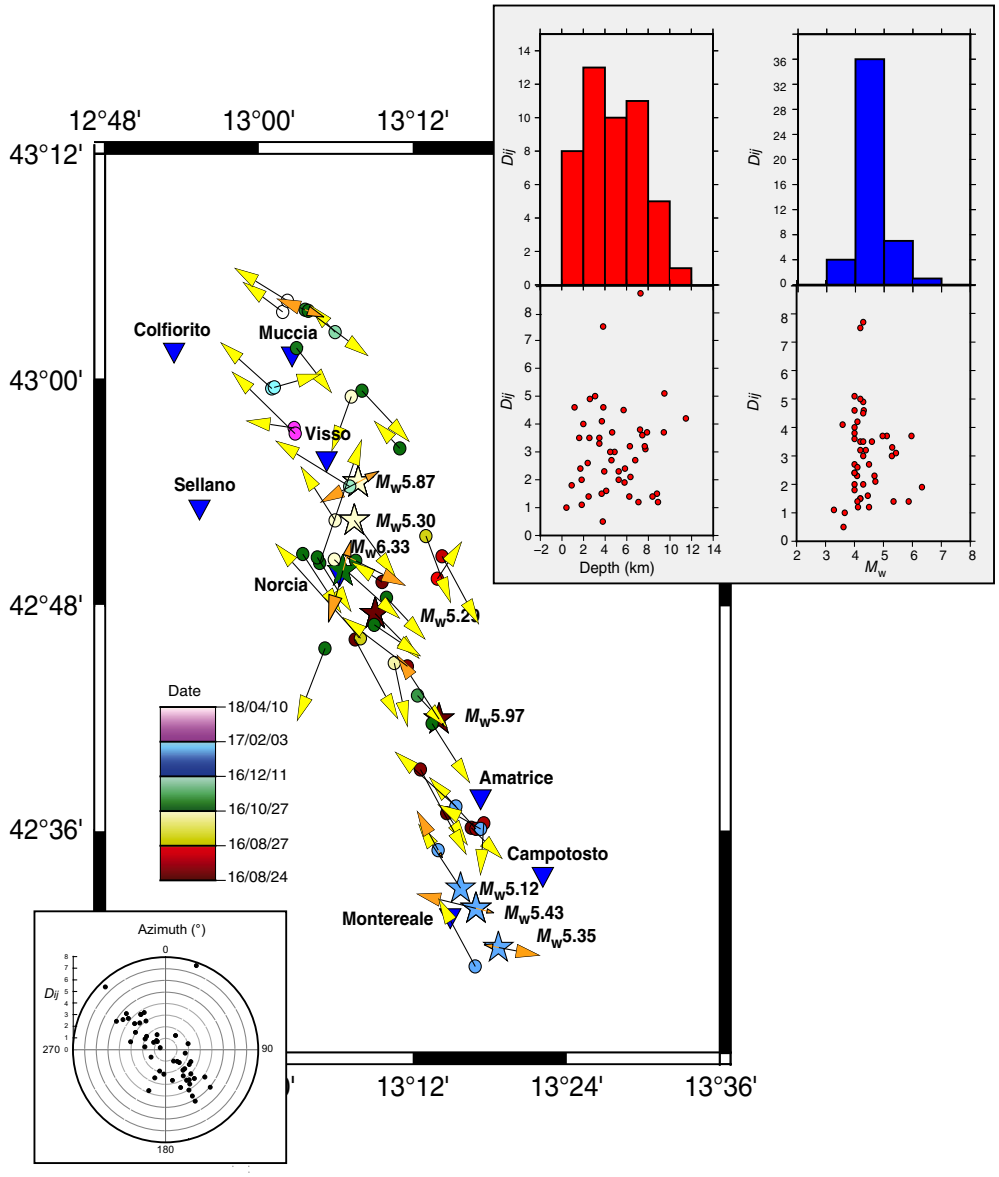

Figure 3. Map of the seismic events analyzed in this study (circles) in color scale showing the time evolution of the seismic sequence. The yellow arrows (D_{index}) point to the rupture propagation directions, whereas the orange arrows point to the direction of the bilateral ruptures. The lengths and dimensions of the yellow and orange arrows are proportional to the directivity index. For bilateral ruptures, the relative percentages in opposite directions are those shown in Table S5. In the inset on top right of the figure, the directivity index trend is shown as a function of magnitude and depth. The inset on the bottom left corner the diagram shows preferred strike of the rupture directions. The color version of this figure is available only in the electronic edition.

varies. To address this, a weighted average (Table S1) was introduced in the analysis.

Results and Discussion

To verify the reliability of our generalized procedure, we compare the results obtained in this study (Tables S3–S5) with those published by Calderoni *et al.* (2017) and Wang *et al.* (2019) for the same seismic sequence. Tables S3 and S4 listed the same results, except for the hypocentral coordinates. In Table S5, we reported the statistical significance of the azimuthal amplitude changes (%) in the bilateral ruptures measured using the D_{index}. For bilateral events, the estimate of the percentage of propagation of the rupture in the opposite along-strike directions are only indicative because of the small number of stations in the FO direction.

For 14 out of 16 seismic events, the rupture propagation direction corresponds to that found by Calderoni *et al.* (2017). In Calderoni *et al.* (2017), two out of 16 events are characterized by a value of $D_{index} < 2$ and then considered isotropic. In addition, in this study for these two low directivity events we evaluate the main rupture propagation direction. For the bilateral seismic events we confirm the same results found in Calderoni *et al.* (2017). We show the heterogeneity of rupture directivity along the activated fault system even if most of the studied events have similar focal mechanisms, that is, normal-faulting ruptures along a northwest–southeast prevailing strike (Fig. 3). We find that there is no correlation between directivity and the depth or magnitude of the events (upper inset in Fig. 3). However, a homogeneous pattern of main rupture directivity is observed along the activated fault system with areas characterized by a predominant rupture direction. We find a clear correlation between the northwest–southeast strike of the main faults and the values of the directivity index (Fig. 3). The diagram in the lower inset of Figure 3 also clearly shows a preferred strike of the rupture directions. The analyzed events are characterized by a predominant northwest–southeast directivity, in agreement with Colavitti *et al.* (2022). In the AVN area, the main northwest–southeast-

striking fault system is crossed by the northeast–southwest Sibillini thrust, which shows a strike roughly orthogonal to that of the central Apennine seismogenic normal faults (Fig. 1). This thrust represents a major crustal discontinuity of the Apennine chain and may, at least in part, control the rupture propagation direction in the AVN sequence, although the available focal mechanisms do not provide evidence for a reactivation of the thrust. In addition, seismic lines, and crustal geophysical models (Retrace 3D, 2021) evidence northwest–southeast-striking, southwest-dipping thrusts with northeast–southwest-striking lateral ramps dissected by the active northwest–southeast-striking normal faults. These thrusts, which include the Sibillini thrust, extend in depth from 10–12 km to about 5–6 km and, in some cases, to the surface. These compressive structures, although not active, act as structural discontinuities within the Apennines and represent zones of weakness that may control the rupture pattern of the large earthquakes. Our data show that sparse northeast–southwest rupture directions in the AVN sequence occur (Fig. 3). As a result, we propose that the thrusts represent "passive" structures able, however, to partly control the rupture directivity of the seismic events located in their neighbors. In the area between Amatrice and Norcia, the predominant rupture direction is toward southeast, whereas north of Norcia and south of Campotosto there is a predominant northwest rupture direction, in agreement with Colavitti *et al.* (2022). In the area extending from Amatrice to Campotosto there is a less homogeneous trend. The bilateral events (Table S5) shown in Figure 3 (orange arrows) seem to be consistent with transition zones between homogeneous areas, characterized by the same direction of rupture propagation. Our results agree well with those of Wang *et al.* (2019), which are obtained through the azimuthal variation of the apparent source spectra (Fig. 4a). For the common events in the top inset of Figure 4a, we show the comparison of the azimuth of the rupture direction propagation. Within the error bars the two results are in a good agreement. For the mainshock, we obtain a directivity percentage of 90% and 10% in the two opposite directions, according to the results of Wang *et al.* (2019). However, Wang *et al.* (2019) also found rupture propagation in the north–south direction and only in a few cases in the Apennine direction, whereas we also find source rupture directivity in anti-Apennine directions, that is, along the strike of the Sibillini thrust and lateral ramps of other minor thrusts. In our method, the solution is stable and does not depend on the chosen frequency range (Fig. S1), whereas in the method of Wang *et al.* (2019) different results are obtained depending on the chosen frequency.

To reasonably interpret our results in light of previous studies on the crustal structure of the epicentral area, in Figure 4b we have overlaid the rupture directivity shown in Figure 3 with the trace of active normal faults of Improta *et al.* (2019) and, in Figure 4c, with the V_P/V_S anomalies by Chiarabba *et al.* (2018). Figure 4b shows that the rupture directivity is mostly consistent with the strike of the main active normal faults and the surface coseismic ruptures. In Figure 4c, we show that the earthquakes with magnitudes greater than 5 have rupture propagation vectors that extend from the zones of low V_P/V_S (high V_S) toward zones of higher V_P/V_S (low V_S) identified by tomographic images at 3 and 6 km depth (Chiarabba *et al.*, 2018). Considering that (a) the high-V_P/V_S values are supposed to be associated with a crustal volume with overpressurized fluids and (b) the direct correlation between the release of carbon dioxide and the number and magnitude of earthquakes observed during AVN seismic sequence (Chiodini *et al.*, 2020), we suggest that fluids moving along the ruptures migrate from zones of high fluid pressure to volumes of lower pressure, these latter located outside the AVN seismic cloud. Different causes have been suggested to justify rupture directivity: the bimaterial fault interface effect (Weertman, 1980; Ben-Zion and Andrews 1998; Ampuero and Ben-Zion, 2008), reversed-polarity secondary deformation structures (Ben-Zion *et al.*, 2012), fault curvature, crustal channeling of waves, persistent stress gradient (Ben-Zion, 2001), or a random phenomenon caused by transient effects such as evolving stresses and/or fluids. Some evidence for preferred directivity of earthquake ruptures (Dor *et al.*, 2006; Lengliné and Got, 2011) is found on the San Andreas fault (Thurber *et al.*, 2006; Lewis *et al.*, 2007; Zhao *et al.*, 2010), the San Jacinto fault (e.g., Scott *et al.*, 1994; Allam and Ben-Zion, 2012; Kurzon *et al.*, 2014), and the North Anatolian fault (e.g., Bulut *et al.*, 2012; Ozakin *et al.*, 2012), where a contrast in seismic velocities was found across the examined fault zone. Lengliné and Got (2011), Kane *et al.* (2013), and Wang *et al.* (2014) inferred that the predominant rupture direction of earthquakes on the San Andreas fault at Parkfield is consistent with a material contrast across the fault, that is, occurrence of bimaterial. The spatial variation of the directivity is stable and cannot be explained by a simple trade-off of rupture velocity or rupture orientation (Abercrombie *et al.*, 2017). Large fault zones have bimaterial interfaces that separate different lithologies. These are generated by long-term offset along the fault, cumulative rock damage products, and other fault-zone-related structures such as basins and mountains. The presence of different rock types within and across fault zones can also alter the properties of local seismic and geodetic fields (e.g., Ben-Zion and Aki, 1990; Le Pichon *et al.*, 2005; Ozeren and Holt, 2010). In our case, drastic changes of lithology along the strike of the whole AVN, northwest–southeast fault system may be excluded (Retrace 3D, 2021), although the possible role of fluids in creating zones of bimaterial defined by the CO_2 saturated fault planes and the surrounding, gas unsaturated rocks cannot be excluded, at least during the seismic sequence. This latter hypothesis is supported by the results of Di Luccio *et al.* (2010) for the 2009 L'Aquila sequence and Chiodini *et al.* (2020) for the AVN sequence. These authors found that the migration of CO_2-rich fluids is involved in the evolution of

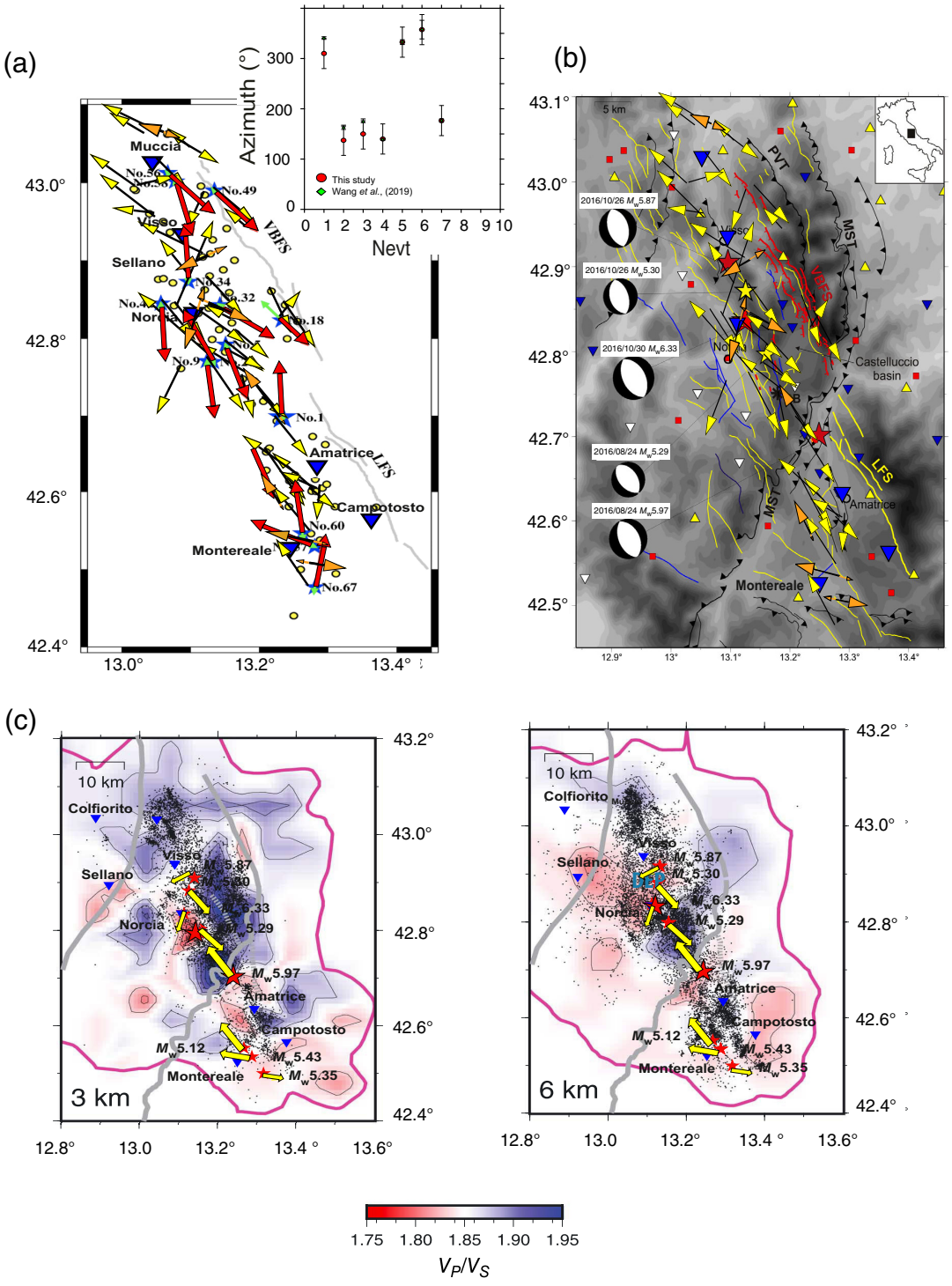

Figure 4. (a) Redrawn from Wang *et al.* (2019) with overlapped directivity index (D_{index}, yellow arrows). The inset in the top right corner shows the comparison between the same seismic events of Wang *et al.* (2019) and this study. (b) Map of the epicentral area showing main active normal faults (redrawn from Improta *et al.*, 2019). Yellow lines represent west-dipping fault, blue lines represent east-dipping faults, yellow bold lines represent Laga fault system, red solid lines represent coseismic surface rupture along the Vettore-Bove fault system, the black barbed lines represent Miocene Pliocene thrust, red stars represent the three mainshocks, and yellow stars represent M 5+ events. Yellow arrows correspond to the directivity index. (c) V_P/V_S layers at 3 (left) and 6 (right) km depth (redrawn from Chiarabba *et al.*, 2018). The aftershocks and mainshocks (stars) occurring at ±1.5 km from each layer are shown. The gray lines are the main thrust of the system and St denotes Sibillini thrust modified from Bigi *et al.* (2011). The dashed lines are the tip of the blind ramps at depth. Magenta line is a well-resolved area. SH, Laga structural high. The seismic events analyzed in this study are superimposed on the four panels. The yellow arrows correspond to the main directions (D_{index}) of the rupture directivity of the seismic events with $M_w > 5$. The yellow arrows point toward the zone with high V_P/V_S (low V_S). The color version of this figure is available only in the electronic edition.

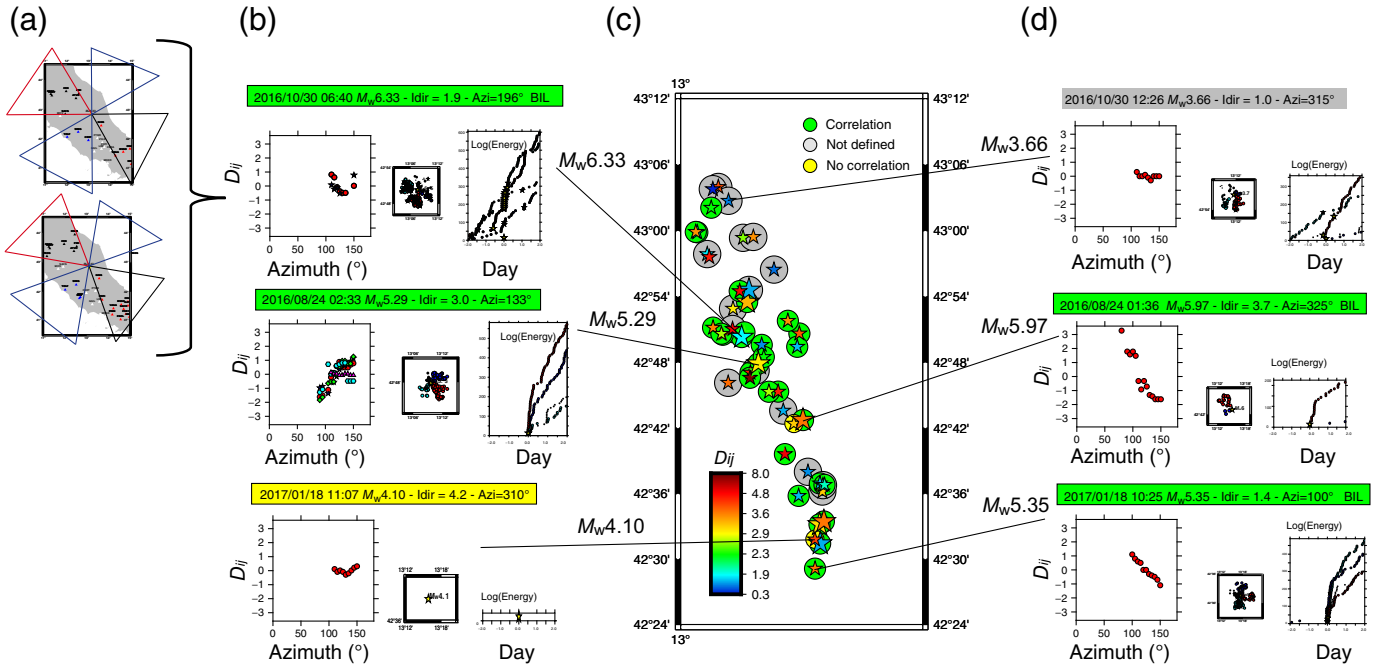

Figure 5. Directivity index (D_{ij}) and cumulative logarithm energy in the space–time windows of 5 km and two days in the forward, backward, and FO rupture directivity propagation, respectively. (a) Map of the stations in the forward (red), backward (black), and FO (blue) directions map of the stations that recorded M_w 6.33 and EGFs pairs of events. (b) Examples of good (green) and no good (yellow) correlation. In the left, D_{ij} versus azimuth for the different EGFs; in the middle, map of the seismic events occurred in the space (5 km) and time (two days) selected intervals; in the right, cumulative logarithm energy in the space (5 km) and time (two days) selected intervals. (c) Map of the seismic events of this study: the star symbols in the green circle correspond to good correlation between the direction of the rupture propagation and the seismicity migration. The star symbols in the gray circle correspond to not define correlation and the star in the yellow circle correspond to not good correlation. (d) Examples of not define (gray) and good (green), same of middle and right sides of panel (b). The color version of this figure is available only in the electronic edition.

the seismic sequences and the fluid paths that occur along the strike of the main faults. Therefore, we propose that these faults and, possibly, pre-existing structural discontinuities be considered as zones of weakness in which the fluids filling the fault gouges during earthquakes can create a bimaterial interface (Brietzke and Ben-Zion, 2006). As a conclusion, the occurrence of pre-existing structural discontinuities as the northwest–southeast active faults and, in a lesser amount, of lateral ramps of inactive thrust, along with the preferred fluid circulation along such structural discontinuities, is responsible for the measured direction of rupture propagation at AVN seismic sequence. In addition, bimaterial fault interfaces can significantly affect the mode, dynamic properties, and propagation direction of earthquake ruptures (e.g., Ben-Zion, 2001; Ampuero and Ben-Zion, 2008; Lengliné and Got, 2011; Calderoni *et al.*, 2015; Calderoni *et al.*, 2017) and produce spatiotemporal variations in seismicity along the fault (e.g., Rubin and Gillard, 2000; Zaliapin and Ben-Zion, 2011). Several studies of the San Jacinto fault zone in recent years (McGuire and Ben-Zion, 2017) have found evidence of contrasts in seismic velocities along with asymmetric damage patterns in the fault zone and additional observations that may result from a preferred rupture propagation direction (signatures of directivity in the time domain, asymmetry of aftershocks along the fault, reversed polarity secondary deformation structures near stepovers). As discussed in Rubin and Gillard (2000), Zaliapin and Ben-Zion (2011), and Calderoni *et al.* (2017), an important issue related to rupture directivity is the relationship between the direction of rupture propagation and seismicity after a mainshock, with the probability of occurrence of earthquakes of significant magnitude being higher in the direction of rupture propagation. In this article, we applied a quantitative method to determine a possible influence of the rupture propagation direction on the location of the immediate aftershocks. We calculated the cumulative number of events that occurred in the forward, backward, and orthogonal rupture propagation directions, in a radius of 5 km (Barchi *et al.*, 2021) and a time interval of two days before and after the occurrence of the target event (Fig. 5). By analyzing the cumulative number of events in the two days preceding the reference event, we exclude those events that occur in areas already affected by previous seismicity, a condition that potentially affects the results of the analysis. In Figure 5 and Figure S2, we have divided the events into three groups. The first group (green label in Fig. 5) shows a good correlation with rupture directivity and seismicity, the second (gray label) shows an undefined correlation due

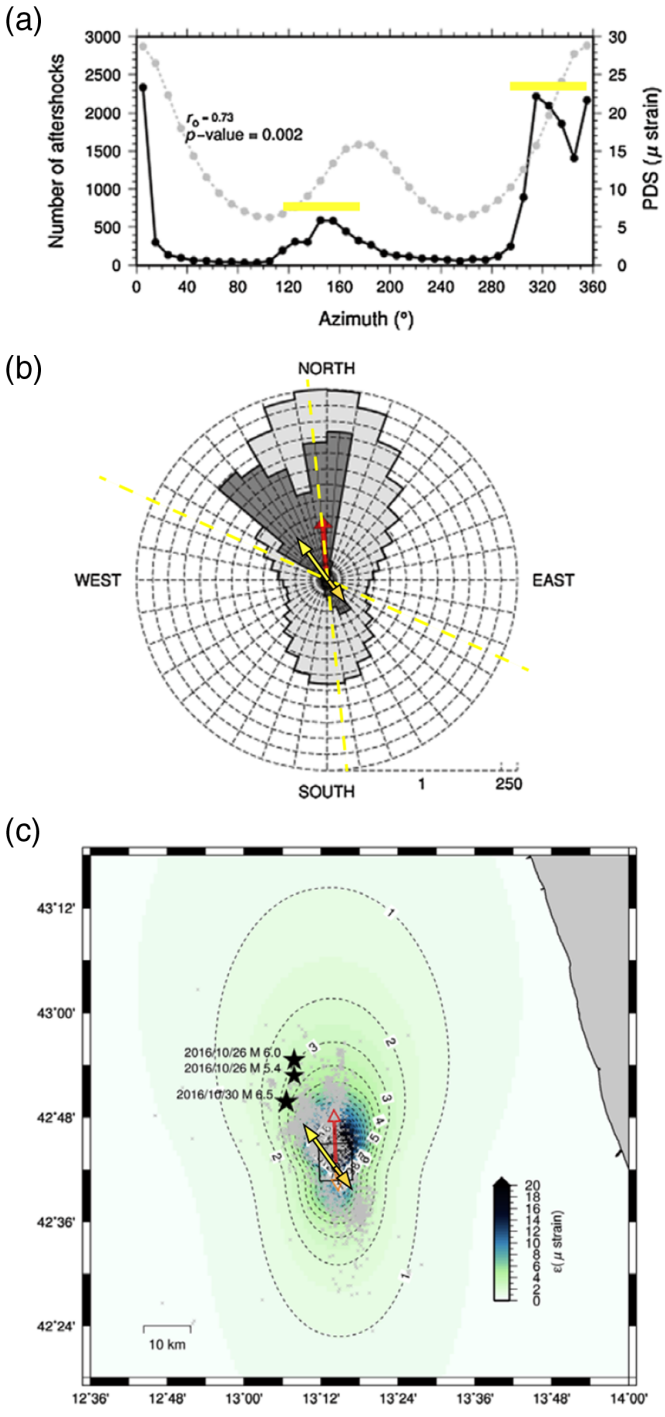

Figure 6. Comparison of our results with those from Convertito *et al.* (2017) for M_w 5.97. (a) Comparison of the number of aftershocks recorded at each azimuth (black dots) and the mean value of peak-dynamic strain (PDS) field (gray dots) for the same azimuth from Convertito *et al.* (2017) with superimposed yellow bars corresponding to the forward and backward rupture propagation direction. (b) Polar histogram of the number of aftershocks and PDS field at each 10°, color is the same as panel (a), with the superimposed yellow and orange arrows corresponding to the bilateral rupture versus the forward and backward directions, respectively. (c) The PDS field with superimposed yellow and orange arrows as in panel (b). The color version of this figure is available only in the electronic edition.

to previous seismicity in the area, and the third group (yellow label) shows no correlation. Of the 47 events analyzed, 17 (47%) were preceded by seismicity (not defined). Of the remaining 30 events, 28 (93%) show a strong correlation between directivity and seismicity, and only two events (7%) do not appear to be correlated. The correlation between the direction of rupture propagation and the location of subsequent events is further evidence of the reliability of our results. As shown in Figure 5b, Table S2, and Figure S1, the results obtained are stable when using different EGFs. In Table S5, we have listed some seismic events characterized by a bilateral rupture. As shown in Figure S2, for some of these events (events 16, 21, and 39) the estimated directivity index is the same for the different target-EGF pairs considering a 180° increment due to the bilaterality of the target event. For the seismic event 12, the directivity index is the same considering the azimuth of the rupture direction of about 330°. Only for three seismic events (events 8, 10, and 18 corresponding to about 6% of the analyzed cases) does this method fail. Further confirmation of the reliability of our estimates was obtained when we overlaid the M_w 5.97 rupture propagation direction with the peak-dynamic strain (Fig. 6a), the distribution of aftershocks (Fig. 6b), and the polar histogram of the number of aftershocks (Fig. 6c) estimated by Convertito *et al.* (2017). In contrast to the estimates of Wang *et al.* (2019) and Convertito *et al.* (2017), we estimate the propagation direction of the rupture for M_w 5.97 to be northwest (325°), and not north (360°), as claimed by the other authors. Figure 6 shows that our estimate is in better agreement with the increase in the number of aftershocks, which is higher in the forward direction and lower in the backward direction (Fig. 6b,c). It is also surprising to observe that the strongest seismic event, M_w 6.33, of the AVN sequence occurred exactly in the estimated of the propagation rupture direction of M_w 5.97 suggested in this study.

Conclusions

We apply a generalized version of the method proposed by Calderoni *et al.* (2017), based on the EGF technique, to estimate the main direction of rupture propagation.

The advantages of our method are its reliability, technical simplicity, and fast application (near real time).

Moreover, the procedure proposed in this study can be applied without knowing a priori the geological–structural characteristics of the area under study and without any need to estimate the crustal attenuation model in advance or make hypotheses on the rupture propagation model. Similarly, to this study, Kurzon *et al.* (2014) used PGV and PGA to estimate rupture directivity, without having any a priori knowledge of the attenuation model. Recently, Kurzon *et al.* (2022) applied the same procedure to the synthetic waveforms generated in numerical rupture simulations, using spectral velocities. We applied our analysis to the 50 $M_w \geq 3.5$ events of the 2016–2017 AVN seismic sequence in central Italy. We found that the

rupture directivity is heterogeneous and shows a complex pattern along the activated normal fault system. The preferred trend of the rupture propagation is controlled mainly by the presence of the fluid in the pre-existing structural discontinuities, (northwest–southeast active faults and the northeast–southwest lateral ramps of older thrusts). The occurrence of fluid pathways within pre-existing structural discontinuities changes the local fault strength and may explain the formation of a bimaterial fault interface. According to Zhang and Jeffrey (2006), the friction effect becomes less important as the fluid penetrates along the horizontal pre-existing fracture, and the injection pressures for different frictional coefficients tend to the same value. Therefore, we suggest that fluid may be the origin of the bimaterial interface in the area affected by the AVN sequence. We also find evidence for the control of rupture directivity on the location of immediate aftershocks. Even though there are only a few events for which we were able to evaluate the correlation between the directivity and the migration of the aftershocks (30 out of 50 events), we found a clear correlation between the directivity and the localization of the immediate aftershocks in 93% of the cases.

Data and Resources

Some of the figures were produced using the Generic Mapping Tool (GMT; Wessel and Smith, 1991). The Seismic Analysis Code (SAC; Goldstein *et al.*, 2003) was used for much of the analysis. The Istituto Nazionale di Geofisica e Vulcanologia (INGV) data are accessible through the European Integrated Data Archive (EIDA; http://eida.rm.ingv.it/it/networks/network/IV) and through the Italian Seismological Instrumental and Parametric Database (ISIDe; http://iside.rm.ingv.it/). The event selection is done via an interactive map for the region shown in Figure 1 and for the selected events listed in Table S2. The list of earthquakes in INGV is available at http://storing.ingv.it/cfti/cfti5/ and http://terremoti.ingv.it/en. The information about determination of moment tensors is available at http://www.eas.slu.edu/eqc/eqc_mt/MECH.IT/. All websites were last accessed in August 2022.

Declaration of Competing Interests

The authors acknowledge that there are no conflicts of interest recorded.

Acknowledgments

Giovanna Calderoni developed this study within the research project Real-time Earthquake Risk Reduction for a Resilient Europe (RISE), Grant Agreement 821115. Rita Di Giovambattista developed this study with funds by a grant from the Italian Ministry of Foreign Affairs and International Cooperation.

References

Abercrombie, R. E. (2014). Stress drops of repeating earthquakes on the SanAndreas Fault at Parkfield, *Geophys. Res. Lett.* **41**, 8784–8791, doi: 10.1002/2014GL062079.

Abercrombie, R. E. (2015). Investigating uncertainties in empirical Green's function analysis of earthquake source parameters, *J. Geophys. Res.* **100,** no. B12, 24015–24036.

Abercrombie, R. E., P. Poli, and S. Bannister (2017). Earthquake directivity, orientation, and stress drop within the subducting plate at the Hikurangi Margin, New Zealand, *J. Geophys. Res.* doi: 10.1002/2017jb014935.

Akinci, A., L. Malagnini, and F. Sabetta (2010). Characteristics of the strong ground motions from the 6 April 2009 L'Aquila earthquake, Italy, *Soil Dyn. Earthq. Eng.* **30,** 320–335.

Allam, A. A., and Y. Ben-Zion (2012). Seismic velocity structures in the southern California plate-boundary environment from double-difference tomography, *Geophys. J. Int.* **190,** no. 2, 1181–1196, doi: 10.1111/j.1365-246X.2012.05544.x.

Ammon, C., A. Velasco, and T. Lay (1993). Rapid estimation of rupture directivity: Application to the 1992 Landers (MS=7.4) and Cape Mendocino (MS=7.2), California earthquakes, *Geophys. Res. Lett.* **20,** no. 2, 97–100, doi: 10.1029/92GL03032.

Ampuero, J.-P., and Y. Ben-Zion (2008). Cracks, pulses and macroscopic asymmetry of dynamic rupture on a bimaterial interface with velocity-weakening friction, *Geophys. J. Int.* **173,** 674–692, doi: 10.1111/j.1365-246X.2008.03736.x.

Barchi, M. R., F. Carboni, M. Michele, M. Ercoli, C. Giorgetti, M. Porreca, S. Azzaro, and L. Chiaraluce (2021). The influence of subsurface geology on the distribution of earthquakes during the 2016–2017 central Italy seismic sequence, *Tectonophysics* **870,** 228797, doi: 10.1016/j.tecto.2021.228797.

Ben-Zion, Y. (2001). Dynamic ruptures in recent models of earthquake faults, *J. Mech. Phys. Solids* **49,** 2209–2244.

Ben-Zion, Y., and K. Aki (1990). Seismic radiation from an SH line source in a laterally heterogeneous planar fault zone, *Bull. Seismol. Soc. Am.* **80,** 971–994.

Ben-Zion, Y., and D. Andrews (1998). Properties and implications of dynamic rupture along a material interface, *Bull. Seismol. Soc. Am.* **88,** 1085–1094.

Ben-Zion, Y., T. Rockwell, Z. Shi, and S. Xu (2012). Reversed-polarity secondary deformation structures near fault stepovers, *J. Appl. Mech.* **79,** 031025, doi: 10.1115/1.4006154.

Bigi, S., P. Casero, and G. Ciotoli (2011). Seismic interpretation of the Laga basin: Constraints on the structural setting and kinematics of the Central Apennines, *J. Geol. Soc.* **168,** no. 1, 179–190, doi: 10.1144/0016-76492010-084.

Billi, A., and M. M. Tiberti (2009). Possible causes of arc development in the Apennines, central Italy, *GSA Bull.* doi: 10.1130/b26335.1.

Boatwright, J. (2007). The persistence of directivity in small earthquakes, *Bull. Seismol. Soc. Am.* doi: 10.1785/0120050228.

Brietzke, G. B., and Y. Ben-Zion (2006). Examining tendencies of in-plane rupture to migrate to material interfaces, *Geophys. J. Int.* **167,** 807–819, doi: 10.1111/j.1365-246X.2006.03137.x.

Bulut, F., Y. Ben-Zion, and M. Bonhoff (2012). Evidence for a bimaterial interface along the Mudurnu segment of the North Anatolian fault zone from polarization analysis of P waves, *Earth Planet. Sci. Lett.* **327/328,** 17–22, doi: 10.1016/j.epsl.2012.02.001.

Calderoni, G., A. Rovelli, Y. Ben-Zion, and R. Di Giovambattista (2015). Along-strike rupture directivity of earthquakes of the 2009 L'Aquila, central Italy, seismic sequence, *Geophys. J. Int.* **203,** 399–415, doi: 10.1093/gji/ggv275.

Calderoni, G., A. Rovelli, and R. Di Giovambattista (2017). Rupture directivity of the strongest 2016–2017 central Italy earthquakes, *J. Geophys. Res.* **122,** doi: 10.1002/2017JB014118.

Carminati, E., and C. Doglioni (2012). Alps vs. Apennines: The paradigm of a tectonically asymmetric Earth, *Earth Sci. Rev.* doi: 10.1016/j.earscirev.2012.02.004.

Chen, P., T. H. Jordan, and L. Zhao (2010). Resolving fault plane ambiguity for small earthquakes, *Geophys. J. Int.* doi: 10.1111/j.1365-246x.2010.04515.x.

Chiarabba, C., P. De Gori, M. Cattaneo, D. Spallarossa, and M. Segou (2018). Faults geometry and the role of fluids in the 2016–2017 central Italy seismic sequence, *Geophys. Res. Lett.* **45,** no. 14, 6963–6971, doi: 10.1029/2018GL077485.

Chiodini, G., C. Cardellini, A. Amato, E. Boschi, S. Caliro, F. Frondini, and G. Ventura (2004). Carbon dioxide Earth degassing and seismogenesis in central and southern Italy, *Geophys. Res. Lett.* **31,** L07615, doi: 10.1029/2004GL019480.

Chiodini, G., C. Cardellini, F. Di Luccio, J. Selva, F. Frondini, and S. Caliro (2020). Correlation between tectonic CO2 Earth degassing and seismicity is revealed by a 10-year record in the Apennines, Italy, *Sci. Adv.* **6,** no. 35, eabc2938 , doi: 10.1126/sciadv.abc2938.

Convertito, V., R. De Matteis, and N. A. Pino (2017). Evidence for static and dynamic triggering of seismicity following the 24 August 2016, $M_w = 6.0$, Amatrice (central Italy) earthquake, *Pure Appl. Geophys.* **174,** 3663–3672, doi: 10.1007/s00024-017-1559-1.

Colavitti, L., G. Lanzano, S. Sgobba, F. Pacor, and F. Gallovič (2022). Empirical evidence of frequency dependent directivity effects from small to-moderate normal fault earthquakes in central Italy, *J. Geophys. Res.* **127,** e2021JB023498, doi: 10.1029/2021JB023498.

Cultrera, G., F. Pacor, G. Franceschina, A. Emolo, and M. Cocco (2008). Directivity effects for moderate-magnitude earthquakes (M_w 5.6–6.0) during the 1997 Umbria–Marche sequence, central Italy, *Tectonophysics* **476,** 110–120, doi: 10.1016/j.tecto.2008.09.022.

Del Gaudio, S., M. Causse, and G. Festa (2015). Broad-band strong motion simulations coupling k-square kinematic source models with empirical Green's functions: The 2009 L'Aquila earthquake, *Geophys. J. Int.* **203,** 720–736, doi: 10.1093/gji/ggv325.

Di Luccio, F., G. Ventura, R. Di Giovambattista, A. Piscini, and F. R. Cinti (2010). Normal faults and thrusts reactivated by deep fluids: The 6 April 2009 Mw6.3 L'Aquila earthquake, central Italy, *J. Geophys. Res.* doi: 10.1029/2009jb007190.

Dor, O., T. K. Rockwell, and Y. Ben-Zion (2006). Geological observations of damage asymmetry in the structure of the San Jacinto, San Andreas and Punchbowl faults in southern California: A possible indicator for preferred rupture propagation direction, *Pure Appl. Geophys.* **163,** 301–349, doi: 10.1007/s00024-005-0023-9.

Douglas, A., J. A. Hudson, and R. G. Pearce (1988). Directivity and the Doppler effect, *Bull. Seismol. Soc. Am.* **78,** 1376–1372.

Fletcher, J. B., and P. Spudich (1998). Rupture characteristics of the three M-4.7 (1992-1994) Parkfield earthquakes, *J. Geophys. Res.* **103,** 835–854.

Folesky, J., J. Kummerow, S. A. Shapiro, M. Häring, and H. Asanuma (2016). Rupture directivity of fluid-induced microseismic events: Observations from an enhanced geothermal system, *J. Geophys. Res.* **121,** no. 11, 8034–8047, doi: 10.1002/2016jb013078.

Frankel, A., and H. Kanamori (1983). Determination of rupture duration and stress drop for earthquakes in southern California, *Bull. Seismol. Soc. Am.* **73,** 1527–1551.

Goldstein, P., D. Dodge, M. Firpo, and L. Minner (2003). SAC2000: Signal processing and analysis tools for seismologists and engineers, in *Invited contribution to "The IASPEI International Handbook of Earthquake and Engineering Seismology"*, W. H. K. Lee, H. Kanamori, P. C. Jennings, and C. Kisslinger (Editors), Academic Press, London, doi: 10.1016/S0074-6142(03)80284-X.

Gorini, A., S. Marcucci, P. Marsan, and G. Milana (2004). Strong motion records of the 2002 Molise, Italy, earthquake sequence and stochastic simulation of the main shock, *Earthq. Spectra* **20,** S65.

Hartzell, S. H. (1978). Earthquake aftershocks as Green's functions, *Geophys. Res. Lett.* **5,** no. 1, 1–4, doi: 10.1029/GL005i001p00001.

Haskell, N. A. (1964). Total energy spectral density of elastic wave radiation from propagating faults, *Bull. Seismol. Soc. Am.* **54,** 1811–1841.

Hough, S. E., and D. S. Dreger (1995). Source parameters of the 23 April 1992 M 6.1 Joshua Tree, California, earthquake and its aftershocks: Empirical Green's function analysis of GEOS and TERRAscope data, *Bull. Seismol. Soc. Am.* **85,** 1576–1590.

Improta, L., D. Latorre, L. Margheriti, A. Nardi, A. Marchetti, A. M. Lombardi, B. Castello, F. Villani, M. G. Ciaccio, F. M. Mele, *et al.* (2019). Multi-segment rupture of the 2016 AmatriceVisso-Norcia seismic sequence (central Italy) constrained by the first high-quality catalog of early aftershocks, *Sci. Rep.* **9,** no. 1, 1–13, doi: 10.1038/s41598-019-43393-2.

Kane, D. L., P. M. Shearer, B. P. Goertz-Allmann, and F. L. Vernon (2013). Rupture directivity of small earthquakes at Parkfield, *J. Geophys. Res.* **118,** 212–221, doi: 10.1029/2012JB009675.

Kurzon, I., V. Lyakhovsky, A. Sagy, and Y. Ben-Zion (2022). Radiated seismic energy and source damage evolution from the analysis of simulated dynamic rupture and far-field seismograms, *Geophys. J. Int.* **231,** no. 3, 1705–1726, doi: 10.1093/gji/ggac279.

Kurzon, I., F. L. Vernon, Y. Ben-Zion, and G. Atkinson (2014). Ground motion prediction equations in the san Jacinto Fault Zone: Significant effects of rupture directivity and fault zone amplification, *Pure Appl. Geophys.* **171,** no. 11, 3045–3081, doi: 10.1007/s00024-014-0855-2.

Lanza, V., D. Spallarossa, M. Cattaneo, D. Bindi, and P. Augliera (1999). Source parameters of small events using constrained deconvolution with empirical Green's functions, *Geophys. J. Int.* **137,** no. 3, 651–662, doi: 10.1046/j.1365-246x.1999.00809.x.

Le Pichon, X., C. Kreemer, and N. Chamot-Rooke (2005). Asymmetry in elastic properties and the evolution of large continental strike-slip faults, *J. Geophys. Res.* **110,** no. B3, doi: 10.1029/2004JB003343.

Lengliné, O., and J. L. Got (2011). Rupture directivity of micro-earthquake sequences near Parkfield, California, *Geophys. Res. Lett.* **38,** L08310 , doi: 10.1029/2011GL047303.

Lewis, M. A., Y. Ben-Zion, and J. McGuire (2007). Imaging the deep structure of the San Andreas Fault south of Hollister with joint analysis of fault-zone head and direct P arrivals, *Geophys. J. Int.* **169,** 1028–1042, doi: 10.1111/j.1365-246X.2006.03319.x.

Malagnini, L., F. P. Lucente, P. GoriDe, A. Akinci, and I. Munafo' (2012). Control of pore fluid pressure diffusion on fault failure mode: Insights from the 2009 L'Aquila seismic sequence, *J. Geophys. Res.* doi: 10.1029/2011jb008911.

Mariucci, M. T., and P. Montone (2020). IPSI 1.4, database of Italian present-day stress indicators, *Istituto Nazionale di Geofisica e Vulcanologia (INGV)*, doi: 10.13127/IPSI.1.4.

McGuire, J. J. (2004). Estimating finite source properties of small earthquake ruptures, *Bull. Seismol. Soc. Am.* doi: 10.1785/0120030091.

McGuire, J., and Y. Ben-Zion (2017). Detailed analysis of earthquake directivity in the San Jacinto Fault Zone, *SCEC Final Rept. Project 16104*, available at https://www.scec.org/proposal/report/16104 (last accessed September 2022).

Miller, S. A., C. Collettini, L. Chiaraluce, M. Cocco, M. Barchi, and B. J. P. Kaus (2004). Aftershocks driven by a high-pressure CO2 source at depth, *Nature* **427,** 724–727, doi: 10.1038/nature02251.

Montone, P., and M. T. Mariucci (2016). The new release of the Italian contemporary stress map, *Geophys. J. Int.* **205,** no. 3, 1525–1531, doi: 10.1093/gji/ggw100.

Mori, J. (1993). Fault plane determinations for three small earthquakes along the San Jacinto Fault, California: Search for cross faults, *J. Geophys. Res.* **98,** no. B10, 17,711–17,722, doi: 10.1029/93JB01229.

Ozakin, Y., Y. Ben-Zion, M. Aktar, H. Karabulut, and Z. Peng (2012). Velocity contrast across the 1944 rupture zone of the North Anatolian fault east of Ismetpasa from analysis of teleseismic arrivals, *Geophys. Res. Lett.* **39,** L0830 , doi: 10.1029/2012GL051426.

Ozeren, S. M., and W. E. Holt (2010). The dynamics of the eastern Mediterranean and eastern Turkey, *Geophys. J. Int.* **183,** doi: 10.1111/j.1365-246X.2010.04819.x.

Pino, N. A., S. Mazza, and E. Boschi (1999). Rupture directivity of the major shocks in the 1997 Umbria–Marche (central Italy) sequence from regional broadband waveforms, *Geophys. Res. Lett.* **26,** 2101–2104, doi: 10.1029/1999GL900464.

Pischiutta, M., A. Akinci, L. Malagnini, and A. Herrero (2016). Characteristics of the strong ground motion from the 24th August 2016 Amatrice Earthquake, *Ann. Geophys.* **59,** Fast Track 5.

Prieto, G. A., R. L. Parker, F. L. Vernon, P. M. Shearer, and D. J. Thomson (2006). Uncertainties in earthquake source spectrum estimation using empirical Green functions, in *Earthquakes: Radiated Energy and the Physics of Faulting*, R. Abercrombie, A. McGarr, G. Di Toro, and H. Kanamori (Editors), Geophysical Monograph Series, Vol. 170, AGU, Washington, D.C., doi: 10.1029/170GM08.

Pucci, S., P. M. De Martini, R. Civico, F. Villani, R. Nappi, T. Ricci, R. Azzaro, C. A. Brunori, and M. Caciagli *et al.* (2017). Coseismic Rupture of the 24 August 2016, M_w 6.0 Amatrice earthquake (central Italy), *Geophys. Res. Lett.* **44,** 2138–2147.

Retrace 3D (2021). RETRACE-3D Central Italy geological model, doi: 10.13127/retrace-3d/geomod.2021.

Ross, Z. E., and Y. Ben-Zion (2016). Toward reliable automated estimates of earthquake source properties from body wave spectra, *J. Geophys. Res.* **121,** no. 6, 4390–4407, doi: 10.1002/2016JB013003.

Rubin, A., and D. Gillard (2000). Aftershock asymmetry/rupture directivity along central San Andreas fault microearthquakes, *J. Geophys. Res.* **105,** 19,095–19,109, doi: 10.1029/2000JB900129.

Scott, J. S., T. G. Masters, and F. L. Vernon (1994). 3-D velocity structure of the San Jacinto Fault zone near Anza, California, *Geophys. J. Int.* **119,** 611–626, doi: 10.1111/j.1365-246X.1994.tb00145.x.

Seekins, L. C., and J. Boatwright (2010). Rupture directivity of moderate earthquakes in Northern California, *Bull. Seismol. Soc. Am.* doi: 10.1785/0120090161.

Thurber, C., H. Zhang, F. Waldhauser, J. Hardebeck, A. Michael, and D. Eberhart-Phillips (2006). Three-dimensional compressional wave speed model, earthquake relocations, and focal mechanisms for the Parkfield, California, region, *Bull. Seismol. Soc. Am.* **96,** no. 4B, 38–S49.

Tinti, E., L. Scognamiglio, A. Cirella, and M. Cocco (2014). Up-dip directivity in near-source during the 2009 L'Aquila mainshock, *Geophys. J. Int.* **198,** 1618–1631.

Tomic, J., R. E. Abercrombie, and A. F. Do Nascimento (2009). Source parameters and rupture velocity of small M≤ 2.1 reservoir induced earthquakes, *Geophys. J. Int.* doi: 10.1111/j.1365-246x.2009.04233.x.

Ventura, G., F. R. Cinti, F. LuccioDi, and N. A. Pino (2007). Mantle wedge dynamics versus crustal seismicity in the Apennines (Italy), *Geochem. Geophys. Geosys.* doi: 10.1029/2006gc001421.

Wang, E., A. M. Rubin, and J. P. Ampuero (2014). Compound earthquakes on a bimaterial interface and implications for rupture mechanics, *Geophys. J. Int.* **197,** no. 2, 1138–1153, doi: 10.1093/gji/ggu047.

Wang, H., Y. Ren, R. Wen, and P. Xu (2019). Breakdown of earthquake self-similar scaling and source rupture directivity in the 2016–2017 central Italy seismic sequence, *J. Geophys. Res.* doi: 10.1029/2018jb016543.

Weertman, J. (1980). Unstable slippage across a fault that separates elastic media of different elastic constants, *J. Geophys. Res.* **85,** 1455–1461.

Wessel, P., and W. H. F. Smith (1991). Free software helps map and display data, *Eos* **72,** 441–448, doi: 10.1029/90EO00319.

Zaliapin, I., and Y. Ben-Zion (2011). Asymmetric distribution of early aftershocks on large faults in California, *Geophys. J. Int.* **185,** 1288–1304.

Zhang, X., and R. Jeffrey (2006). The role of friction and secondary flaws on deflection and re-initiation of hydraulic fractures at orthogonal pre-existing fractures, *Geophys. J. Int.* **166,** 1454–1465, doi: 10.1111/j.1365-246X.2006.03062.x.

Zhao, P., Z. Peng, Z. Shi, M. A. Lewis, and Y. Ben-Zion (2010). Variations of the velocity contrast and rupture properties of M6 earthquakes along the Parkfield section of the San Andreas fault, *Geophys. J. Int.* **180,** 765–780, doi: 10.1111/j.1365-246X.2009.04436.x.

Manuscript received 4 October 2022
Published online 10 April 2023